

Supporting Information

Synergistic Interplay between Oxygen-Vacancy and S-Scheme Charge Transfer Dynamics in LaFeO₃/FeOOH Heterojunction Towards Sono Assisted Photo Fenton Antibiotic Degradation and Water Splitting

Anshumika Mishra¹, Newmoon Priyadarshini¹, Kulamani Parida*¹

¹*Centre for Nano Science and Nano Technology,
S 'O' A (Deemed to be University), Bhubaneswar—751 030, Odisha (India)*

***Corresponding Author**

kulamaniparida@soauniversity.ac.in & paridakulamani@yahoo.com

Text S1. Experimental section

S1.1. Materials and Methods

La(NO₃)₃·6H₂O (99.99%, AR), Fe(NO₃)₃·9H₂O (≥99%), FeSO₄·7H₂O (≥99%), C₆H₈O₇·H₂O (≥99%), CH₃COONa·3H₂O (≥99%), NH₄OH, AgNO₃, FeCl₃, ofloxacin, and Nafion were procured from Sigma-Aldrich. DI water was used to make all the aqueous solutions. All reagents used are of analytical grade and employed without any additional purification.

S1.1.1. Synthesis of LaFeO₃ nanoparticles

The LFO nanoparticles were synthesized by adopting a similar sol-gel method reported earlier in the literature [1], wherein, the raw materials taken were La(NO₃)₃·6H₂O, Fe(NO₃)₃·9H₂O, NH₄OH, & C₆H₈O₇·H₂O. Following a molar ratio of 1:1:2, the calculated mass of La(NO₃)₃·6H₂O, Fe(NO₃)₃·9H₂O, & C₆H₈O₇·H₂O were suspended in DI water under magnetic stirring. A uniform nitrate-citrate sol was created. The pH was adjusted to 7 by adding NH₄OH to stabilize the sol, followed by stirring the sol overnight at 60°C and gradually increasing the temperature to 130°C, forming a dried gel, which finally underwent calcination at 500°C for 2 h to obtain pure LFO.

S1.1.2. Synthesis of FeOOH

The FeOOH photocatalysts were synthesized at room temperature via the coprecipitation method. 5 mmol of FeSO₄·7H₂O, 10 mmol of CH₃COONa·3H₂O, and 50 mL of deionized water were stirred at 40 °C for 6 hours. A reddish-orange precipitate was obtained and washed with ethanol-water solution, followed by centrifugation. The resulting product was then heated at 60 °C for 12 hours in an oven to yield the FeOOH catalyst.

S1.1.3. In-situ synthesis of LFO/FeOOH heterostructure

LFO@FeOOH binary heterostructures were prepared in varying ratios of 1:1, 1:2, 1:3, and 1:4 via the in situ coprecipitation method with varied amounts of prepared LFO. In a standard procedure, the binary 1:1 heterostructure is prepared by adding 5 mmol of FeSO₄·7H₂O and 10 mmol of CH₃COONa·3H₂O to 100 mL of DI water under continuous stirring for 15 minutes. This is followed by adding 0.19 g of prepared LFO to the above solution and allowed to stir for another 6 h at 40 °C. A reddish-orange precipitate was formed and washed with an ethanol-water mixture before being centrifuged. The obtained product was then dried in an oven at 60°C for 12 h to produce the catalyst LF11. Similar 1:2 (LF12), 1:3 (LF13), & 1:4

(LF14) heterostructures were prepared following the above procedure by adding 0.095, 0.063, and 0.047 g of LFO, respectively. No unusual hazards were observed during the catalyst preparation process.

Text S1.2. Material Characterization

The structural and crystallographic characteristics of the prepared photocatalysts were examined using a Rigaku Ultima-IV X-ray diffractometer (PXRD) with Cu K α radiation. Surface morphology, elemental distribution, and color mapping were investigated through scanning electron microscopy (SEM) on a CARL-ZEISS EVO-18 model operated at an EHT of 20 kV. For insights into internal structural features, transmission electron microscopy (TEM) was performed using a Philips Tecnai G2, with high-resolution TEM (HRTEM) imaging at an accelerating voltage of 200 kV. Surface texture characterization has been achieved using a Quantachrome NOVA-2200e instrument. X-ray photoelectron spectroscopy (XPS) was carried out using a VG-Microtech-Multilab ESCA-3000 with Mg K α radiation to assess the electronic structure and chemical states. Raman spectroscopy measurements, performed with a RENISHAW spectrometer, utilized a 520 nm laser for vibrational analysis. UV-vis DRS (Ultraviolet-visible diffuse reflectance spectroscopy) data were collected on a JASCO 750 spectrophotometer, using BaSO₄ as a reference and a scanning speed of 40 nm/min across the 200–800 nm wavelength range. Steady-state photoluminescence (PL) measurements were acquired on a JASCO FP8300 spectrofluorometer with a 350 nm excitation wavelength. Time-resolved photoluminescence (TRPL) profiles were recorded with a HORIBA SCIENTIFIC DeltaPro Fluorescence Lifetime System, utilizing a 360 nm laser source. Additionally, all photoelectrochemical (PEC) tests were conducted in a three-electrode configuration on an IVIUM-n-STAT multichannel electrochemical workstation.

Text S2. Procedure of Ofloxacin Degradation

Initially, three batches of 20 ml of 20 ppm solution of OFL were dark-stirred with 10 mg of the photocatalyst. A fixed amount of H₂O₂ was then added to the mixture solution. The mixture solutions in the 1st batch were subjected to simulated solar light; in the 2nd batch, US waves were applied, and the 3rd batch was put through both simulated solar light and US waves for 1 h each. For the experimental setup, a Vis-LED photoreactor having a 20 W power Lamp and an Ultrasonicator with a frequency of 40kHz and 150 W power were used. The mixture solutions were centrifuged, and the decant was set to record the absorbance spectra. Absorbance spectra of the 20 ppm OFL solution were also recorded. Comparing the above two

spectra for each degradation batch gives the quantity of OFL degraded under simulated solar light, US waves, and both simulated solar light and US waves.

Ultrasound-Assisted O₂ Evolution Experiment.

For a typical OER, 0.02 g of the catalyst is dispersed in 20 mL of AgNO₃ (0.05 M) solution and continuously stirred in the dark (30 min) to establish adsorption-desorption equilibrium. To remove dissolved O₂, the solution is bubbled with N₂ gas for about 20 min before the OER experiment. The resulting suspension is then subjected to ultrasonication and light illumination simultaneously using a 125 W Hg lamp (0.027 W cm⁻²) and an Ultrasonicator with a frequency of 40 kHz and 150 W power. For these experiments, the reactor was placed inside the ultrasonic bath to favor the generation of O₂. The evolved O₂ is analyzed using an Agilent 7890B-series gas chromatograph equipped with a 5A molecular sieve column and a thermal conductivity detector (TCD). The same procedure is also performed using a FeCl₃ solution.

Text S3. Photoelectrochemical (PEC) measurement

Preparation of FTO (working electrode): The synthesized sample is drop-cast onto the conductive fluorine-doped tin oxide (FTO) glass, which undergoes an initial ultrasonic treatment in a solution of deionized (DI) water and ethanol for 45 minutes before drying at 80°C. A solution is prepared for coating by dispersing 1 mg of the sample in a mixture of 1.6 ml DI water, 40 μL of Nafion, and 1.4 ml ethanol. This solution is applied to the FTO surface. All photoelectrochemical (PEC) measurements are performed in a three-electrode configuration using the IVIUMn-STAT multi-channel electrochemical workstation, with an electrochemical cell setup that includes the FTO-coated sample (working electrode), a platinum - Pt (counter electrode), and a saturated Ag/AgCl reference electrode. These electrodes are immersed in a 0.1 M Na₂SO₄ electrolyte solution (pH ~ 6.5) for the measurements. The coated area of the FTO working electrode is 1 cm², and the bare FTO shows no photocurrent response under light exposure. The setup is illuminated with a xenon (Xe) lamp to study the photoinduced carrier dynamics and measure photocurrent.

Electrochemical Impedance Spectroscopy (EIS) offers valuable insights into the charge transfer resistance and material conductivity during catalytic reactions. EIS measurements span a frequency range from 106 Hz to 0.01 Hz, i.e., Nyquist plots for LFO, FeOOH, and LF13 were analyzed in Na₂SO₄ solution (0.1 M) at an applied potential of 0.0 V. This technique specifically probes the electrical characteristics at the semiconductor/electrolyte interface within photocatalytic systems, facilitating the analysis of charge transfer dynamics between

two photocatalysts. It also helps differentiate phenomena occurring at various rates, such as electron-hole recombination, transport resistances, and series resistances, as well as electron lifetime in materials like LFO and FeOOH. The photocurrent densities of the as-prepared samples are also evaluated via linear sweep voltammetry (LSV) within a 0.5 to 1.5 V potential bias range.

Mott-Schottky (MS) analysis was conducted at 500 Hz with a 25 mV AC voltage to further investigate the band edge alignment and charge transfer mechanism within these materials. This approach provided insights into the flat band potentials ($E_{\text{ne}\beta}$) of the materials. The $E_{\text{ne}\beta}$ values, crucial for understanding the band structure and exciton dynamics in semiconductors, were determined by extrapolating the $C^{-2} = 0$ intercept from MS plots. The flat band potentials for LFO (-0.73 V) and FeOOH (-0.51 eV) were established relative to the Ag/AgCl reference electrode and can be converted to the NHE scale using the Nernst equation

$$E_{\text{NHE}} = E_{\text{Ag/AgCl}} + E_{\text{Ag/AgCl}}^{\circ} + 0.059 (7 - \text{pH}) \quad (\text{S1})$$

At 25 °C, $E_{\text{Ag/AgCl}}^{\circ} = 0.197$ V, where $E_{\text{Ag/AgCl}}$ represents the potential applied of the Ag/AgCl electrode, with an electrolytic pH of 6.5. For n-type semiconductors, E_{fb} typically lies between 0.1 to 0.3 eV below the conduction band minimum (CBM). Assuming a 0.1 eV offset, the conduction band energies for LFO and FeOOH were found as -0.83 eV and -0.61 eV on the NHE scale, respectively. Using their band gaps derived from UV-DRS spectra, the VB (valence band) values were calculated as 1.06 eV for LFO and 1.34 eV for FeOOH on the NHE scale, applying the equation

$$E_{\text{VB}} = E_{\text{g}} + E_{\text{CB}} \quad (\text{S2})$$

Text S4. Radical Tests

To identify the primary ROS — namely electrons (e^{-}), holes (h^{+}), superoxide radicals ($\bullet\text{O}_2^{-}$), and hydroxyl radicals ($\bullet\text{OH}$) — involved in the OFL degradation through an S-P-FP mechanism, quenching experiments were conducted using specific ROS trapping agents. These agents include p-benzoquinone (PBQ) for capturing $\bullet\text{O}_2^{-}$, IPA (isopropyl alcohol) for $\bullet\text{OH}$, citric acid (CA) for h^{+} , and DMSO (dimethyl sulfoxide) for e^{-} . The sequence of reactive species contributing to OFL degradation is as follows: $\bullet\text{O}_2^{-} > \bullet\text{OH} > e^{-} > h^{+}$, indicating the participation of $\bullet\text{O}_2^{-}$ and $\bullet\text{OH}$ radicals play the most significant roles in the degradation process. To confirm

$\bullet\text{O}_2^-$ radicals produced by the samples, a nitroblue tetrazolium (NBT) test was performed. The peak absorbance at 260 nm represents the presence of Formazan, formed by the reaction of NBT with $\bullet\text{O}_2^-$ in the molar ratio 4:1.

The terephthalic acid (TA) test is commonly utilized as a probe molecule for detecting hydroxyl radicals ($\bullet\text{OH}$) due to its reaction with $\bullet\text{OH}$, which produces a characteristic fluorescence emission peak at 425 nm representing the 2-hydroxyterephthalic acid (HTA). By measuring the fluorescence intensity of the above fluorescence spectrophotometer with a 315 nm excitation source, the concentration of $\bullet\text{OH}$ radicals was confirmed.

Text S5. Parameters affecting the degradation process

To assess the impact of inorganic scavengers on pollutant degradation, several anionic scavengers—specifically NaCl, Na_2CO_3 , and NaNO_3 (each at a concentration of 0.05 M)—are employed to examine the influence of anions. This can be explained as follows: (i) Radicals produced by reactions between ROS and anions like Cl^- , CO_3^{2-} , and NO_3^- generally exhibit lower oxidation potentials than hydroxyl radicals, affecting pollutant degradation rates. (ii) Anions in solution may also block the active sites on the LF13 catalyst and scavenge the ROS responsible for the degradation performance. The anions follow the $\text{CO}_3^{2-} > \text{NO}_3^- > \text{Cl}^-$ trend, where Cl^- known to exhibit the lowest scavenging effect. The Cl^- functions as a scavenger for $\text{HO}\bullet$. However, the resulting intermediate ($\text{ClOH}\bullet^-$) may either regenerate the $\text{HO}\bullet$ radical or interact with hydrated electrons (e_{aq}^-) and H_3O^+ ions, ultimately producing $\text{Cl}\bullet$ radicals. which in turn, helps to eliminate $\text{H}\bullet$ and e_{aq}^- species from the reaction medium. Also, a substantially high concentration of Cl^- ions is required to react with $\text{HO}\bullet$ [2]. Additionally, the role of various cationic scavengers—such as CaCl_2 , KCl , and $\text{Mg}(\text{NO}_3)_2$ —is analyzed through the use of corresponding salts. Cations like Ca^{2+} and Mg^{2+} reduce photocatalytic efficiency, likely by altering ionic strength. Some inhibition may result from the complexation of these cations with pollutant molecules on the catalyst surface, with their impact ranked as follows: $\text{Mg}^{2+} > \text{Ca}^{2+} > \text{K}^+$ [2]. This could also be attributed to the decreasing hydrated ionic radius from K^+ to Mg^{2+} , resulting in a slower ion exchange rate than K^+ [3]. Lastly, oxidizing agents, including H_2O_2 and $\text{K}_2\text{S}_2\text{O}_8$, are tested to assess their influence on degradation efficiency, where not much difference is observed as the $\text{HO}\bullet$ responsible for the ofloxacin degradation is produced by the addition of both the oxidizers. Moreover, upon adding persulfate, $\text{HO}\bullet$ generation predominates at higher alkaline levels, introducing the inhibition phenomenon with lower rate constants [4, 5].

A gas sparging study has also been conducted to study the impact of dissolved gases in the Ofloxacin degradation system. Three key properties of gases can significantly affect Sono-Photo-Fenton activity: (1) higher values of ‘polytropic ratio’ increase the intensity of bubble collapse, raising local temperature and pressure; (2) lower ‘thermal conductivity’ limits heat loss during collapse, enhancing temperature and catalytic efficiency; and (3) more excellent ‘solubility in water’ boosts free radical generation by increasing nucleation sites, facilitating cavitation and enhancing the generation of ROS. Hence, catalytic degradation of 20-ppm Ofloxacin solution with 20 mg of catalyst individually purged with Argon (Ar), Oxygen (O₂), and Nitrogen (N₂) into the solution, and the reaction proceeded for one hour. Notably, the Ar-purged system achieved the highest - 92% degradation, following the trend – Ar > O₂ > N₂, likely due to Ar’s relatively high solubility in water (0.056 mL⁻¹), a polytropic ratio of 1.67, and small thermal conductivity of 0.018 W m⁻¹ K⁻¹. In comparison, degradation efficiencies dropped to 86% with O₂ and 80% with N₂, attributed to their lower solubilities (0.049 & 0.015 mL⁻¹, respectively), the polytropic ratio of 1.40, and miniature thermal conductivities of 0.0263 & 0.0258 W m⁻¹ K⁻¹. The introduction of Ar gas enhances the cavitation effects by creating new nucleation points, thereby promoting free radical formation [6].

The impact of pH on the reaction was investigated by adjusting the solution's pH by adding 1M HCl or 1M NaOH to the mixture containing 20 mg of the catalyst and a 20 ppm Ofloxacin solution. To understand the underlying mechanisms, PZC (Point of Zero Charge) determination employing the drift method [7] was conducted on the binary hybrid (Figure S8). The model pollutant, Ofloxacin, has two pKa values of 6.05 and 8.22 [8]; thus, at pH levels below 6.05, it predominantly exists in a cationic state (OFL⁺), while at pH values above 8.22, it transitions to an anionic form (OFL⁻). Between these pKa values, Ofloxacin exists as a zwitterion (OFL⁰). At lower pH levels (pH < pHPZC ~ 4.52), the surface of the catalyst is positively charged, and at pH > pHPZC, the surface is negatively charged. Hence, a sturdy electrostatic attraction exists among the negatively charged catalyst surface and the positively charged and Zwitter ionic OFL (pH = 4.52 – 8.22). Therefore, the S-P-FR degradation performance of the model pollutant OFL follows the trend pH 5 > pH 7 > pH 3 > pH 9, following the above science. Conversely, at elevated pH (3 & 9), the catalyst and OFL acquire positive and negative charges, respectively, resulting in electrostatic repulsion and reduced catalytic activity.

To investigate the degradation products, Liquid Chromatography (LC) and Mass Spectrometry (MS) analyses were performed using an Agilent 6890 and Agilent 5973,

respectively, with the fragmentation results illustrated in Fig. 8. For the kinetic analysis during the degradation experiments, aliquots (2 mL) of the reaction mixture were regularly withdrawn, filtered. The absorbance of the supernatant was measured using a UV-Vis spectrophotometer. Control experiments were conducted under ultrasonic and light conditions without adding LF13 and another with LF13 present but without US and light exposure (Figure S9).

Text S6. Optoelectronic features analysis

The UV-Vis DRS are obtained using a JASCO 750 UV-visible spectrophotometer, with Barium sulfate (BaSO_4) as the reference material. Measurements are conducted across the 200–800 nm wavelength range at a 40 nm per minute scanning rate. The optical band gap (E_g) is calculated according to the Kubelka-Munk function, as described by Equation S3.

$$\alpha h\nu = A (h\nu - E_g)^{n/2} \quad (\text{S3})$$

Where h = Planck's constant, ν = frequency of incident light, α = proportionality-constant, E_g = optical band-gap of material, and A = absorption-coefficient. 'n' denotes various electronic transitions like $n = 1$: direct transition (allowed), and $n = 3$: direct transition.

Text S7. Kinetic Studies using the Langmuir-Hinshelwood model

The kinetic studies of the observed catalytic activity toward OFL degradation are investigated using the Langmuir-Hinshelwood (L-H) model. According to the model, the reaction rate (r) is evaluated with the Equation S4.

$$r = -\frac{dC}{dt} = \frac{kKC}{1 + KC} \quad (\text{S4})$$

When $KC \ll 1$, $\Rightarrow r = -\frac{dC}{dt} = kKC$

But $kK = K_{app}$, $\therefore r = -\frac{dC}{dt} = K_{app}C$

Rearranging the above, $\Rightarrow r = \frac{dC}{C} = -K_{app} dt$

Integrating both sides from time 0 to t ,

$$\Rightarrow \int_{C_0}^{C_t} \frac{1}{C} dC = -K_{app} \int_0^t dt$$

$$\Rightarrow \ln \frac{C_t}{C_0} = -K_{app} t$$

$$\therefore r = \ln \frac{C_0}{C_t} = K_{app} t \quad (S5)$$

Hence, the L-H model reduces to the pseudo-first-order kinetics expression (Equation S5) at

very low concentrations of OFL (20 ppm), where the plot of $\ln C_0/C_t$ against time 't', whose slope gives the value of K_{app} . Following the above method, the calculated k_{app} , R^2 , and $t_{1/2}$ values for the nanomaterials are summarized in Table S1.

Table S1. OFL degradation Efficiencies, R^2 , K_{app} , and $t_{1/2}$ values of all synthesized samples via different processes.

Process	Photocatalyst	DE (%)	R^2	K_{app} (10^{-3}min^{-1})	$t_{1/2}$ (min)
Sono-Photo-Fenton	Blank	-	0	0	-
	LFO	55	0.913	8.04	86
	FeOOH	65	0.912	10.52	65
	LF11	70	0.912	12.29	56
	LF12	82	0.914	15.05	46
	LF13	92.3	0.913	21.95	32
	LF14	80	0.911	13.91	50
Photo-Fenton	Blank	-	0	0	0
	LFO	42	0.910	6.32	109
	FeOOH	45	0.912	6.37	108
	LF11	54	0.909	8.54	81
	LF12	58	0.912	9.83	70
	LF13	50	0.913	8.06	85
	LF14	42	0.913	6.3	110
Sono Fenton	Blank	-	0	0	0
	LFO	50	0.911	7.36	94

	FeOOH	45	0.913	6.55	105
	LF11	54	0.911	8.17	84
	LF12	50	0.910	7.28	95
	LF13	47	0.913	6.8	101
	LF14	40	0.911	5.52	125

Table S2. Comparison of the Degradation performances reported of Ofloxacin.

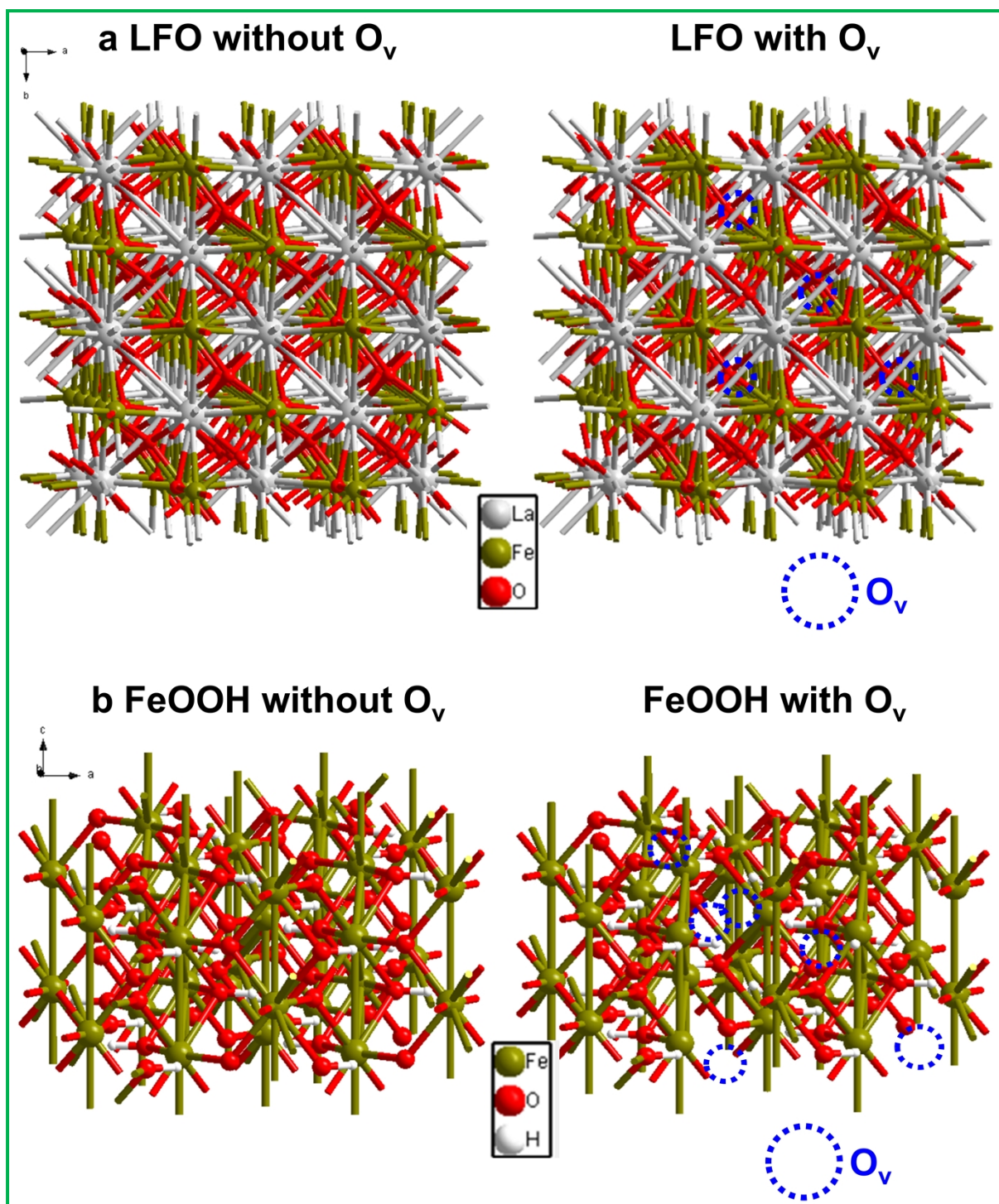
Catalyst	Method	Source	Reaction time (min)	Experimental Conditions	% DE	Ref.
LaFeO ₃	PMS activation	--	--	Catalyst dose = 20 mg OFL = 10 ppm	15	[9]
BaTiO ₃ /CuO	Piezocatalytic	--	120	Catalyst dose = 10 mg OFL = 30 ppm	83	[10]
EBFO-3	Fenton-like + PMS	--	19	Catalyst dose = 25 mg OFL = 10 ppm	22.35	[11]
MIP-PDI/g-C ₃ N ₄	Photocatalysis	300 W	100	Catalyst dose = 50 mg OFL = 10ppm	92	[12]
RPGM	Fe activated persulfate	--	--	OFL = 20 ppm	96.91	[13]
CuFe-LDHs	Persulfate activation	--	120	Catalyst dose = 0.5 g L ⁻¹ OFL = 10 ppm	80	[14]
CoOOH/LaFe _{0.5} Ni _{0.5} O ₃	PMS activation	--	15	OFL = 20 ppm	91.84	[15]
Hem/Fe ₂ TiO ₅	Photocatalysis	--	60	Catalyst dose = 0.5 g L ⁻¹ OFL = 50 ppm	50	[16]

Fe ₃ O ₄ /g-C ₃ N ₄	Photocatalysis + Rotating Magnetic field	2 A RMF	300	1g L-1/3 mg L-1/	87.4	[17]
LFO/FeOOH	Sono-Photo- Fenton	Solar Light + 40 kHz	60	10 mg/ 20 ppm	92.3	This work

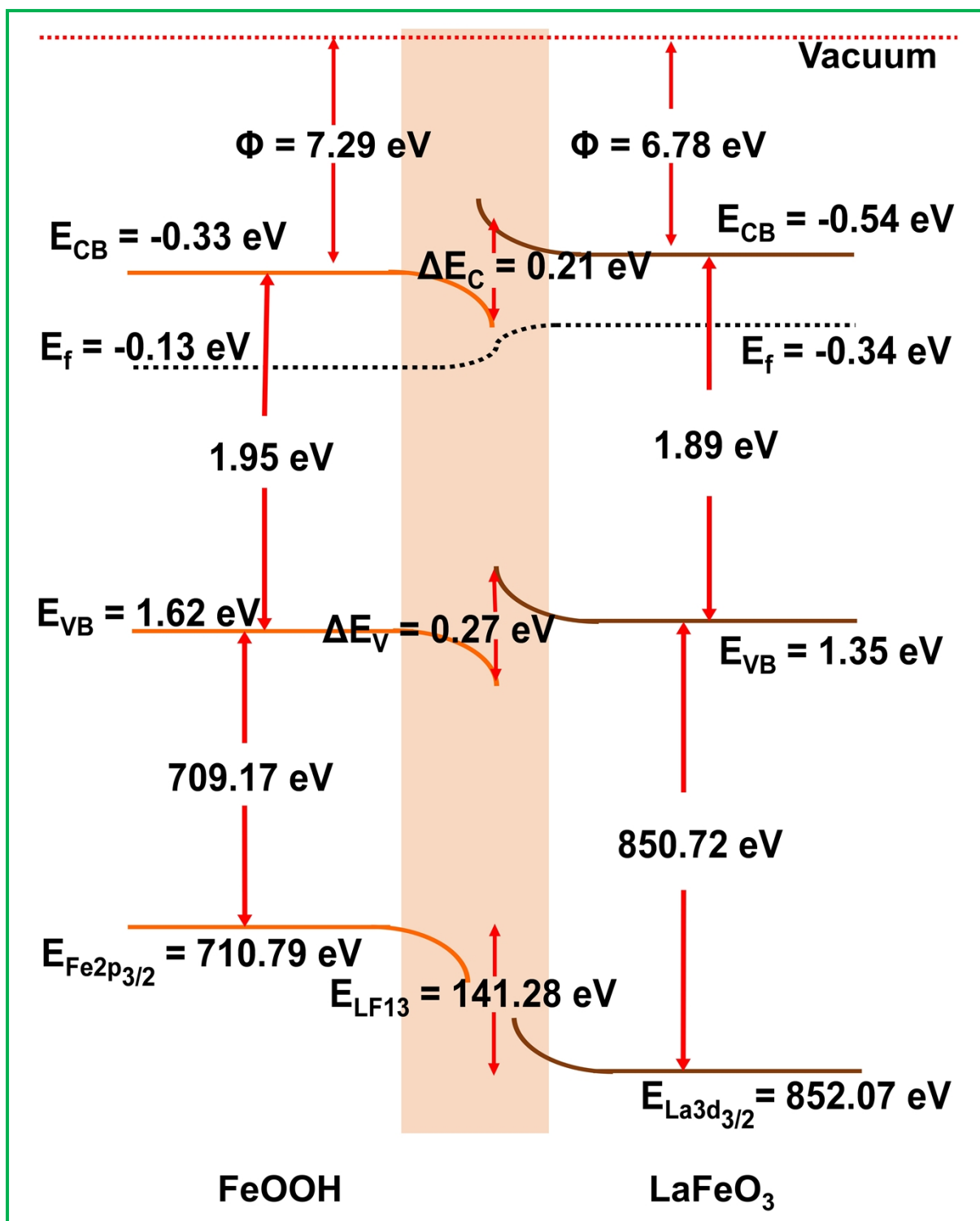
Table S3. Comparison of the OER performances reported for different catalysts.

Catalyst	Method	Source	Catalyst Dose / Sacrificial Agent	Time (h)	Yield	Ref.
LFO	Photocatalysis	125 W Hg Vis lamp	50 mg / 50 ml 10 vol% AgNO ₃	1	640 μmol g ⁻¹	[18]
LFO/RGO	Photocatalysis	125 W Hg Vis lamp	50 mg / 50 mL of 10 vol.% of AgNO ₃	1	316.24 mmol g ⁻¹	[19]
LFO/RGO/NiO	Photocatalysis	125 W Hg Vis lamp	50 mg / 50 ml 10 vol % methanol	1	465 μmol g ⁻¹	[20]
α-FeOOH	Photocatalysis	300W Xe lamp	100 mg / 100 ml water	12	4.7 μmol	[21]
FeOOH/BiVO ₄	Photocatalysis	300W Xe lamp	100 mg / 100 mL 0.02 M NaIO ₄	6	723 μmol	[22]
FeOOH/CdS	Photocatalysis	300W Xe lamp	20 mg / 50 mL 0.1 M NaOH	1	676.50 μmol	[23]
α- FeOOH/CeO ₂ NS	Photocatalysis	150W Xe lamp	20 mg / 20 mL 0.05M AgNO ₃ /FeCl ₃	2	485 μmol	[24]

FeOOH/BiOBr	Photocatalytic	--	100 mg / 100 ml DI water with 1.0 g AgNO ₃	1	284.34 μmol	[25]
NaNbO ₃ /FeOOH	Piezophotocatalysis	125W Hg lamp 40 kHz 100 W	15 mg / 15 ml 0.05 M FeCl ₃	1	1155 μmol g ⁻¹	[6]
LFO/FeOOH	Sono-Photo-Catalysis	125 W Xe lamp, 40 kHz	20 mg / 20 ml 0.05 M FeCl₃	1	1270 μmol	This work



Scheme S1. Formation of Ovs in LFO and FeOOH



Scheme S2. Band offset at LFO/FeOOH heterointerface.

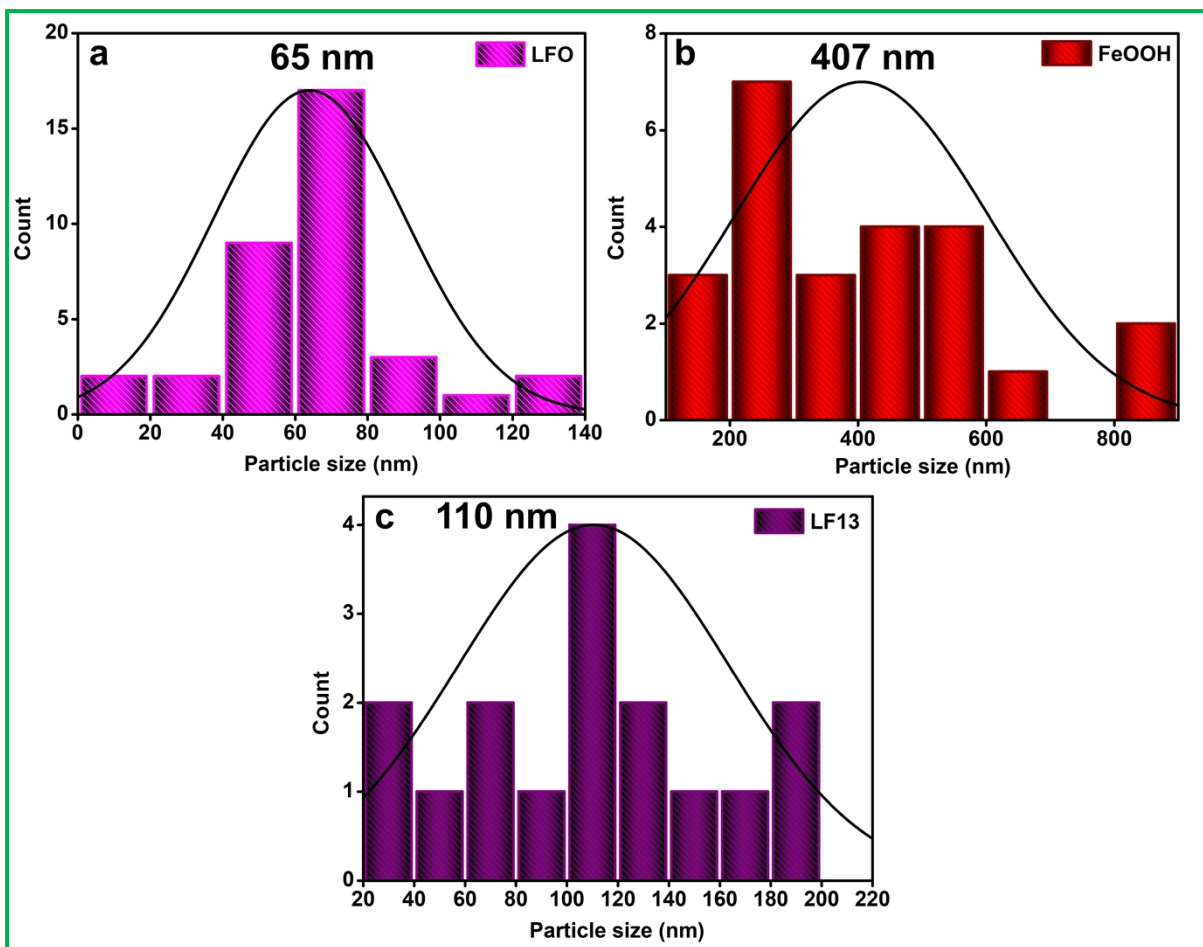


Figure S1. Average particle size determination of (a) LFO, (b) FeOOH, and (c) LF13 from their respective Histograms.

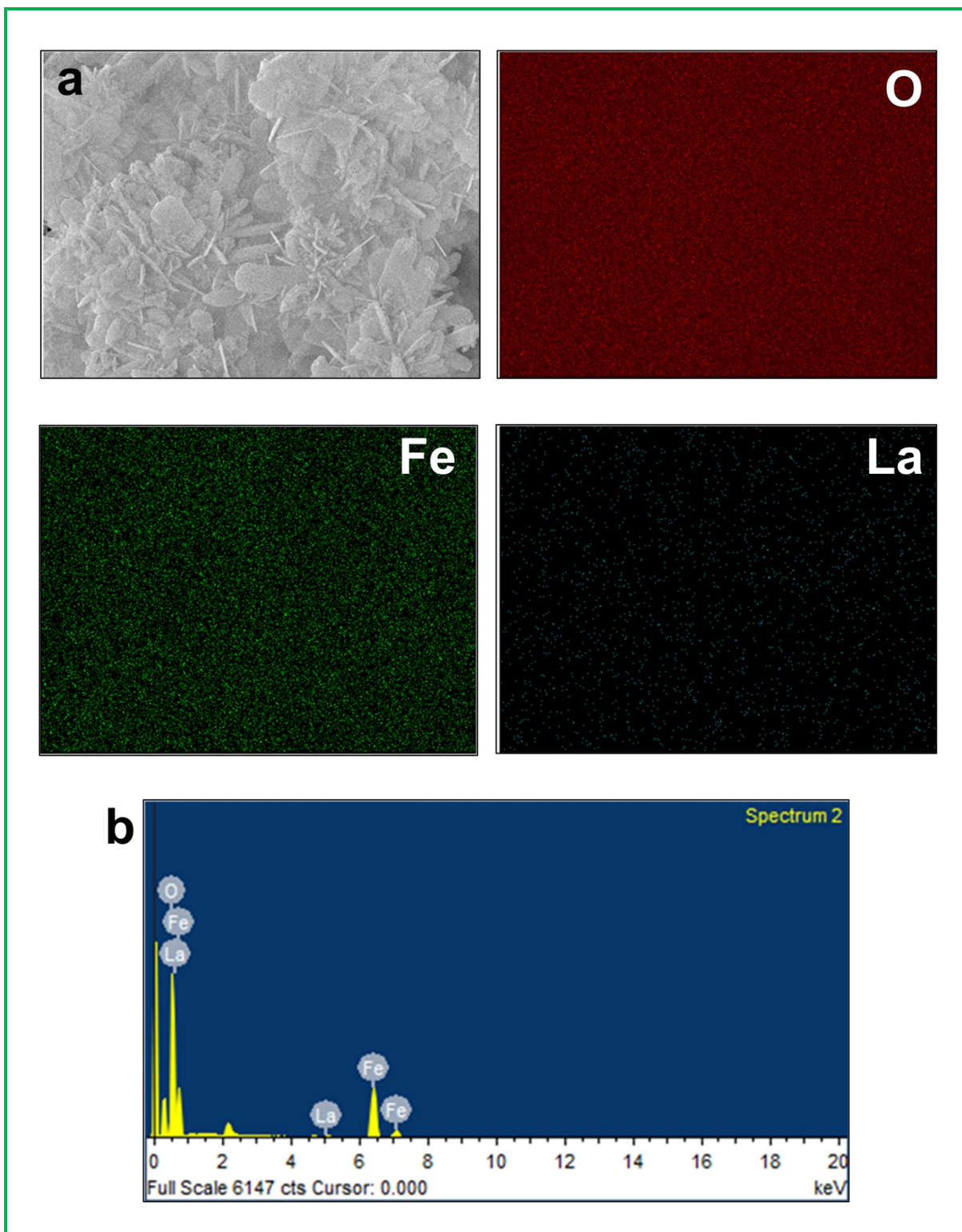


Figure S2. (a) Color mapping and (b) EDAX spectra of nanocomposite LF13.

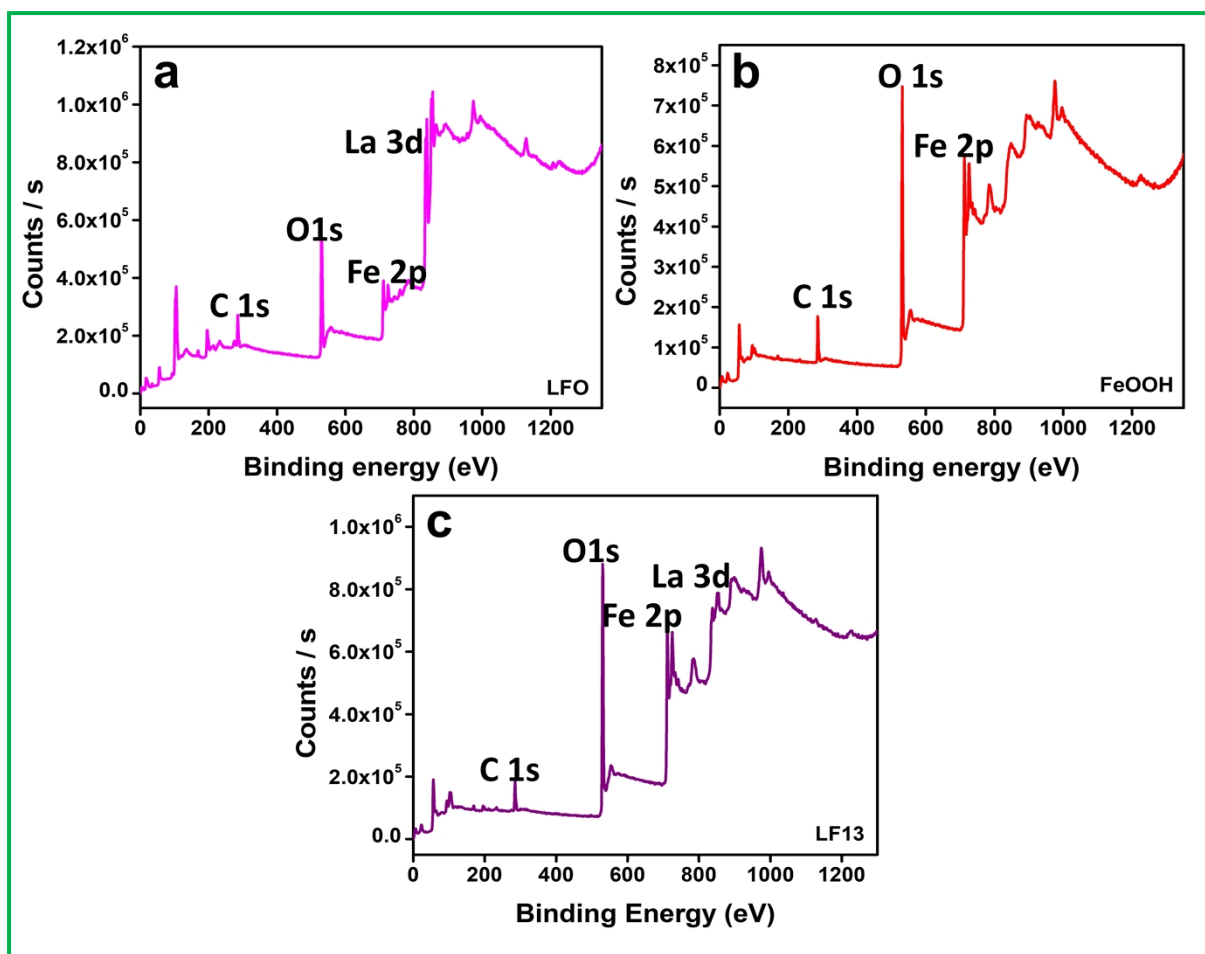


Figure S3. The XPS survey spectra for (a) LFO, (b) FeOOH, and (c) LF13.

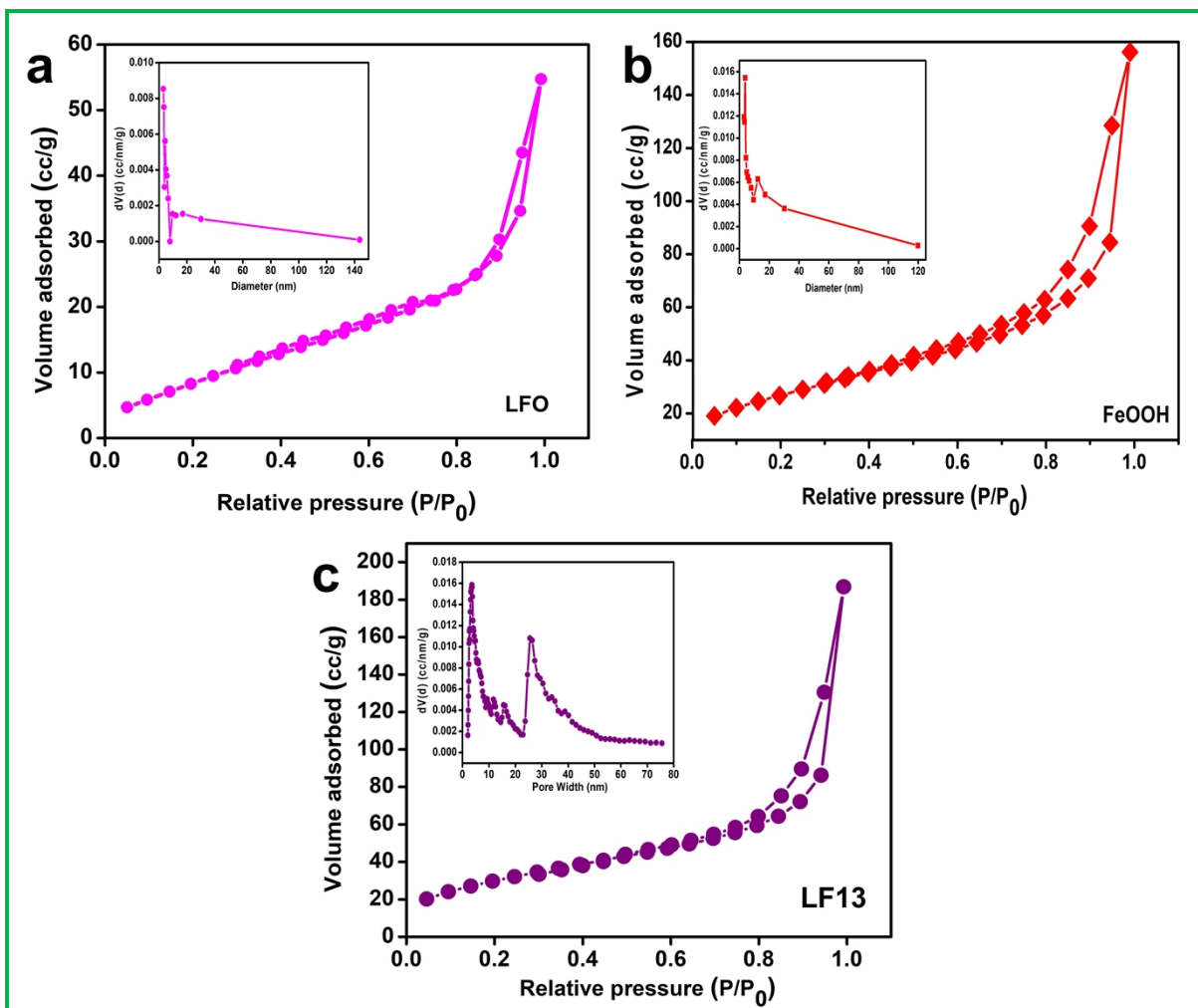


Figure S4. (a-c) BET surface area and pore size (inside) for LFO, FeOOH, and LF-13, respectively.

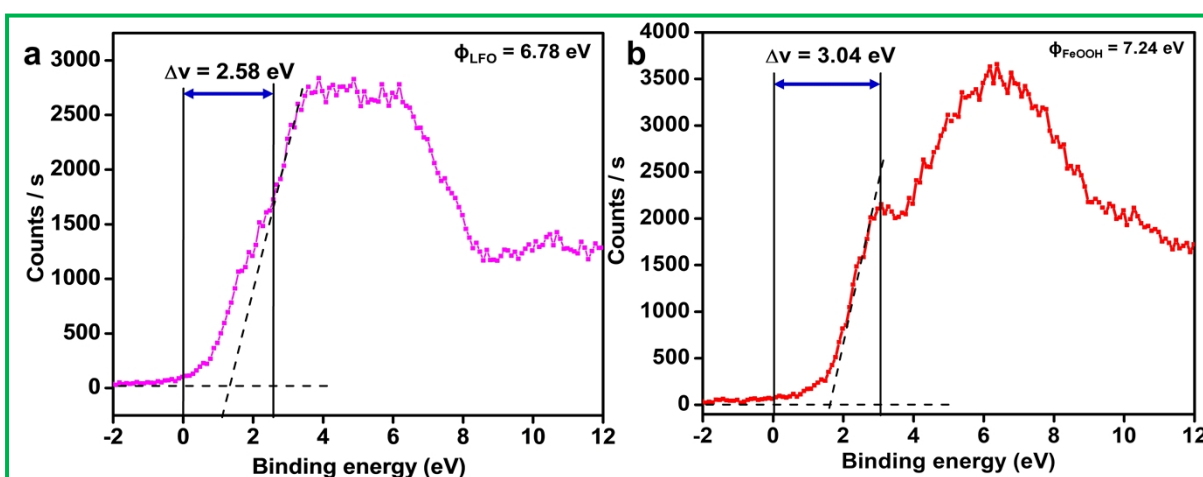


Figure S5. (a-b) Work function determination of the pristine materials from the VB-XPS spectra.

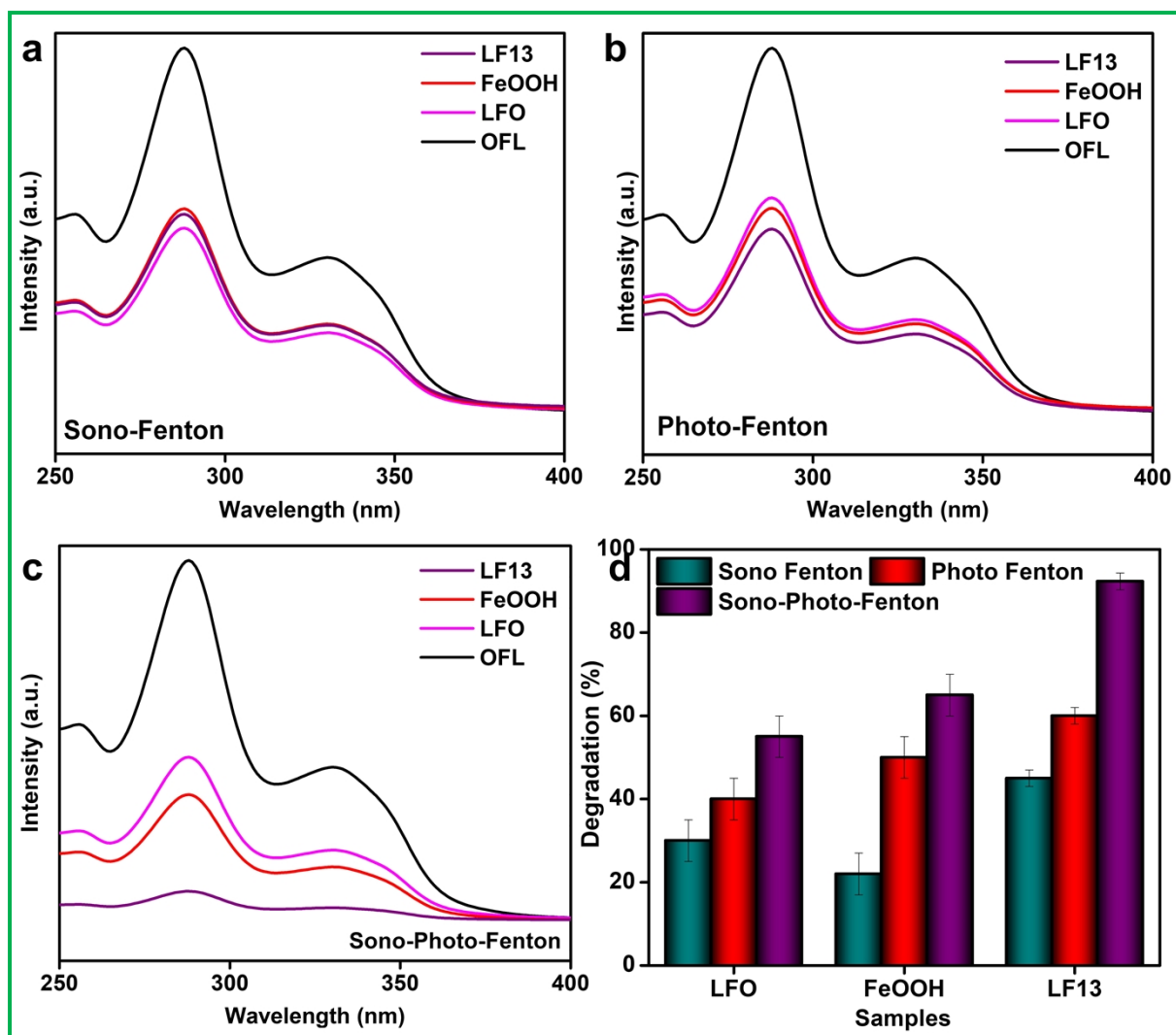


Figure S6. The (a-c) absorbance spectra for Sono Fenton, Photo Fenton, and Sono-Photo-Fenton degradation of OFL, and its corresponding (d) comparative plot.

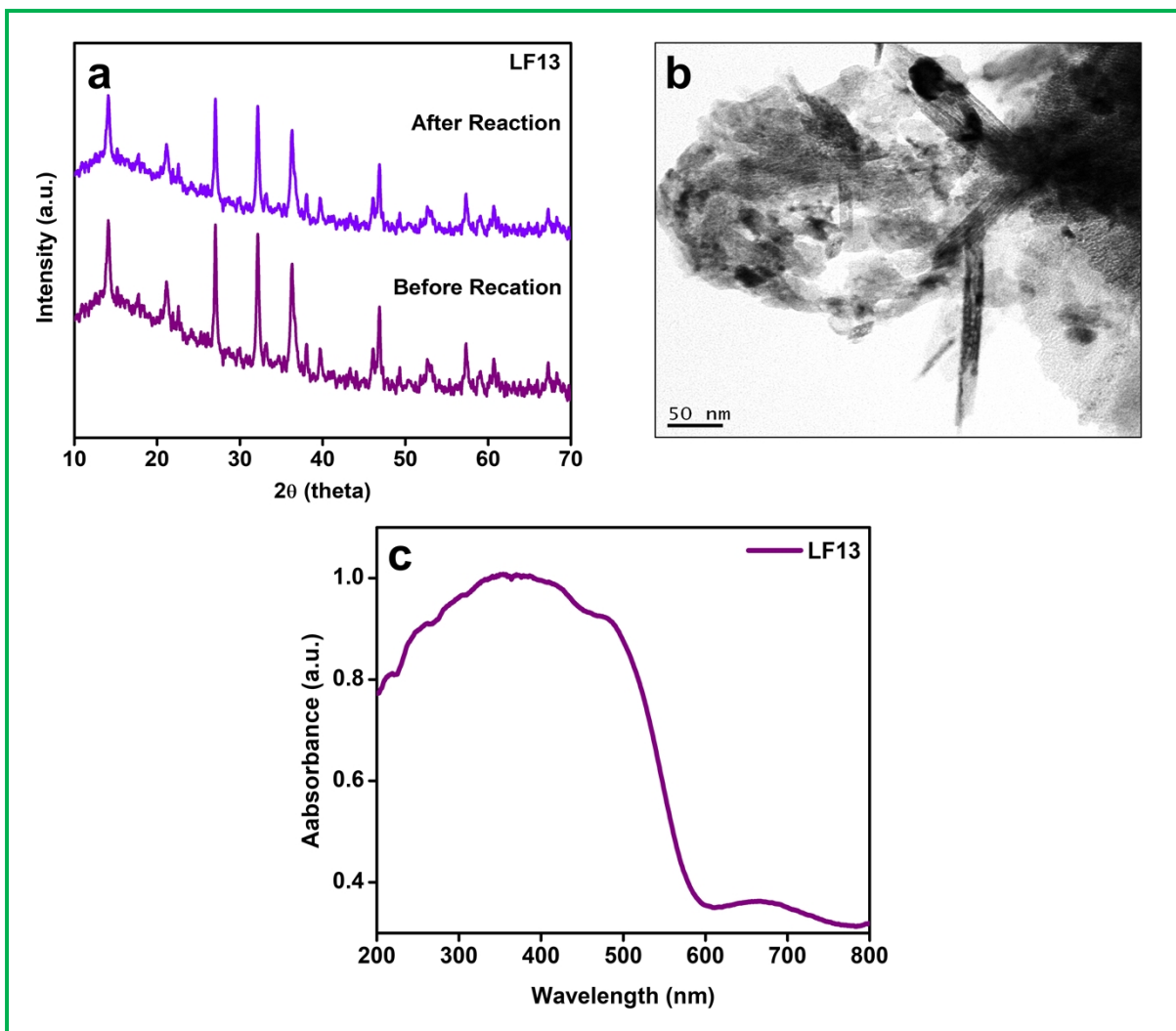


Figure S7. The before and after reaction images of (a) PXRD, (b) HR-TEM, and (c) Absorbance spectra for the best nanocomposite LF13.

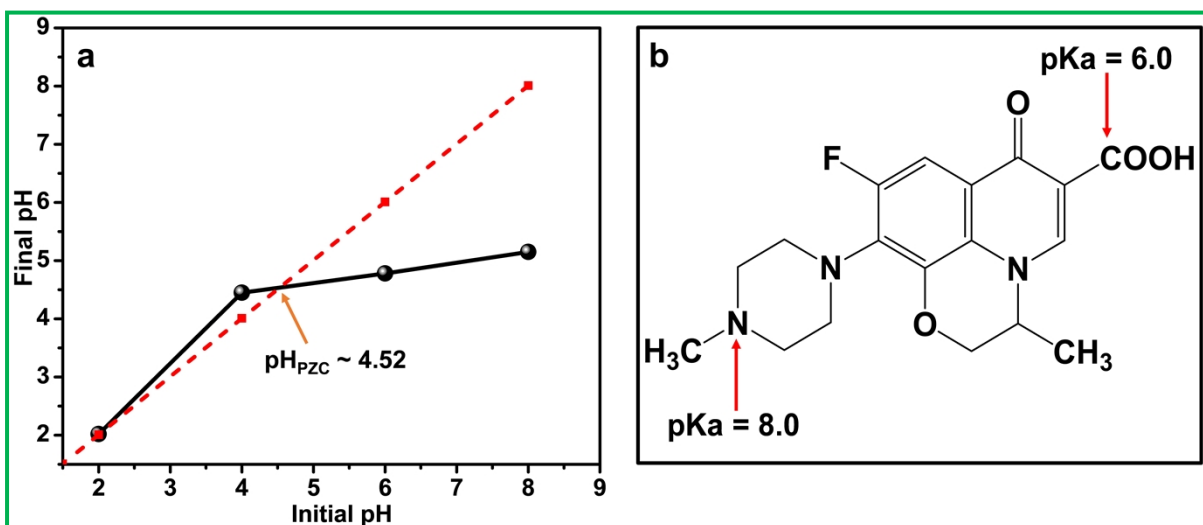


Figure S8 The (a) Point of Zero Charge (PZC) and the (b) pKa representation of Ofloxacin.

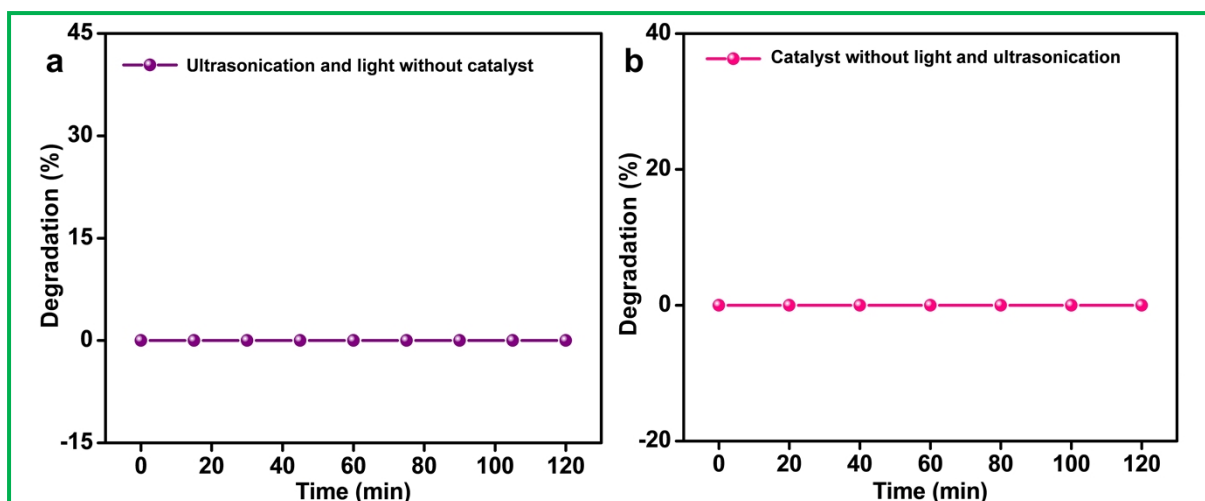


Figure S9. Control experiments of OFL degradation efficiency (a) under ultrasonication and light but without catalyst, and (b) with catalyst but without light and ultrasonication.

References

1. Cen, L., Yu, F., Luo, Y., Li, C., Liu, G., Jin, W., ... & Guo, Y. (2025). *Recyclable biomimetic flower membranes for ofloxacin degradation by peroxymonosulfate activation under visible-light*. *Separation and Purification Technology*, 359, 130620.
2. Ocampo-Pérez, R., et al., *Degradation of antineoplastic cytarabine in aqueous solution by gamma radiation*. *Chemical Engineering Journal*, 2011. **174**(1): p. 1-8.
3. Liu, X., et al., *Degradation difference of ofloxacin and levofloxacin by UV/H₂O₂ and UV/PS (persulfate): Efficiency, factors and mechanism*. *Chemical Engineering Journal*, 2020. **385**.
4. Wang, Y., & Hong, C. S. (1999). *Effect of hydrogen peroxide, periodate and persulfate on photocatalysis of 2-chlorobiphenyl in aqueous TiO₂ suspensions*. *Water Research*, 33(9), 2031-2036.
5. Chen, L., et al., *Degradation of acetamiprid in UV/H₂O₂ and UV/persulfate systems: A comparative study*. *Chemical Engineering Journal*, 2018. **351**: p. 1137-1146.
6. Priyadarshini, N., et al., *Macroscopic Spontaneous Piezopolarization and Oxygen-Vacancy Coupled Robust NaNbO(3)/FeOOH Heterojunction for Pharmaceutical Drug Degradation and O(2) Evolution: Combined Experimental and Theoretical Study*. *Inorg Chem*, 2024. **63**(1): p. 256-271.

7. Kandi, D., et al., *CdS QDs-Decorated Self-Doped gamma-Bi(2)MoO(6): A Sustainable and Versatile Photocatalyst toward Photoreduction of Cr(VI) and Degradation of Phenol*. ACS Omega, 2017. **2**(12): p. 9040-9056.
8. Sakore, S., Choudhari, S., & Chakraborty, B. H. A. S. W. A. T. (2010). *Biowaiver monograph for immediate release solid oral dosage forms: ofloxacin*. Int J Pharm Pharm Sci, 2(Suppl 4), 156-161.
9. Gao, P., et al., *Promoted peroxymonosulfate activation into singlet oxygen over perovskite for ofloxacin degradation by controlling the oxygen defect concentration*. Chemical Engineering Journal, 2019. **359**: p. 828-839.
10. Singh, R., et al., *Ultrasound-activated piezocatalytic degradation of Rhodamine B, Ofloxacin, and inactivation of E. coli by BaTiO3/CuO nanocomposites*. Journal of Environmental Chemical Engineering, 2024. **12**(6).
11. Huang, J., et al., *Eu A-site partial substitution of BiFeO3 as a catalyst for enhanced ofloxacin degradation via singlet oxygen-dominated peroxymonosulfate activation*. Separation and Purification Technology, 2025. **358**.
12. Shi, H., et al., *Preferential degradation of ofloxacin on all-organic molecularly imprinted PDI/g-C3N4 photocatalyst via specific molecular recognition*. Separation and Purification Technology, 2025. **353**.
13. Wang, C., et al., *Effective degradation of ofloxacin using nano-zero-valent iron activated persulfate supported by the reusable porous gel microsphere*. Separation and Purification Technology, 2024. **331**.
14. Zhang, X., et al., *The performance and mechanism of persulfate activated by CuFe-LDHs for ofloxacin degradation in water*. Environmental Science: Nano, 2024. **11**(8): p. 3563-3573.
15. Wang, Y., et al., *Boosting catalytic activity of Fe-based perovskite by compositing with Co oxyhydroxide for peroxymonosulfate activation and ofloxacin degradation*. Colloids and Surfaces A: Physicochemical and Engineering Aspects, 2025. **705**.
16. Wang, W., Guo, J., Zhang, Y., Lu, K., Xu, J., Li, J., ... & Mailhot, G. (2024). *Constructing dual sulfite-mediated processes via inner-sphere complexation and photogenerated carrier modulation with Hematite/Fe2TiO5 heterojunction for ofloxacin degradation*. Applied Catalysis B: Environment and Energy, 358, 124374..
17. Ding, N., Zhang, S., Zhang, J., Zhan, Y., Wang, B., Liu, H., ... & Sun, Y. (2024). *Enhanced ofloxacin degradation in water by a novel integrated photocatalysis and rotating magnetic field system*. Journal of Water Process Engineering, 65, 105874.

18. Parida, K.M., et al., *Fabrication of nanocrystalline LaFeO₃: An efficient sol–gel auto-combustion assisted visible light responsive photocatalyst for water decomposition*. International Journal of Hydrogen Energy, 2010. **35**(22): p. 12161-12168.
19. Acharya, S., D.K. Padhi, and K.M. Parida, *Visible light driven LaFeO₃ nano sphere/RGO composite photocatalysts for efficient water decomposition reaction*. Catalysis Today, 2020. **353**: p. 220-231.
20. Vijayaraghavan, T., et al., *Visible light active LaFeO₃ nano perovskite-RGO-NiO composite for efficient H₂ evolution by photocatalytic water splitting and textile dye degradation*. Journal of Environmental Chemical Engineering, 2021. **9**(1).
21. Wang, T., et al., *X-Shaped alpha-FeOOH with Enhanced Charge Separation for Visible-Light-Driven Photocatalytic Overall Water Splitting*. ChemSusChem, 2018. **11**(8): p. 1365-1373.
22. Zhang, Y., et al., *The improvement of photocatalysis O₂ production over BiVO₄ with amorphous FeOOH shell modification*. Sci Rep, 2019. **9**(1): p. 19090.
23. Li, L., et al., *Oxygen-vacancy-assisted construction of FeOOH/CdS heterostructure as an efficient bifunctional photocatalyst for CO₂ conversion and water oxidation*. Applied Catalysis B: Environmental, 2021. **293**.
24. Sultana, S., S. Mansingh, and K.M. Parida, *Rational design of light induced self healed Fe based oxygen vacancy rich CeO₂ (CeO₂NS–FeOOH/Fe₂O₃) nanostructure materials for photocatalytic water oxidation and Cr(vi) reduction*. Journal of Materials Chemistry A, 2018. **6**(24): p. 11377-11389.
25. Xie, F., et al., *Amorphous FeOOH-mediated directional charges transfer in light-switchable oxygen vacancies BiOBr for boosting photocatalytic oxygen evolution*. Separation and Purification Technology, 2024. **328**.